ACS APPLIED MATERIALS & INTERFACES

Research Article

www.acsami.org

Novel Nanostructures of Rutile Fabricated by Templating against Yarns of Polystyrene Nanofibrils and Their Catalytic Applications

Ping Lu and Younan Xia*

The Wallace H. Coulter Department of Biomedical Engineering, School of Chemistry and Biochemistry, and School of Chemical and Biomolecular Engineering, Georgia Institute of Technology, Atlanta, Georgia 30332, United States

Supporting Information

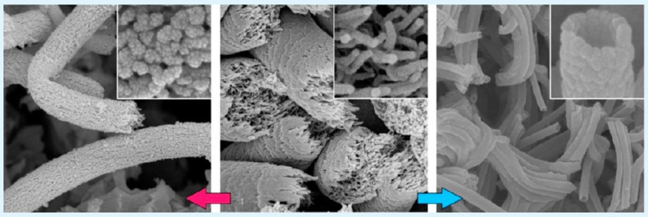

ABSTRACT: This Article describes a facile approach to the synthesis of rutile nanostructures in the form of porous fibers or bundles of nanotubes by maneuvering the surface wettability of yarns made of polystyrene nanofibrils. Specifically, hierarchically porous fibers were obtained by hydrolyzing titanium tetraisopropoxide to form TiO_2 nanoparticles in the void spaces among hydrophobic nanofibrils in each yarn. After calcination in air at 800 °C, the resultant fibers were comprised of many interconnected rutile nanoparticles whose diameters were in the range 20−80 nm. After converting the nanofibrils and yarns into hydrophilic surfaces through plasma treatment, however, the TiO_2 formed conformal coatings on the surfaces of nanofibrils in each yarn during hydrolysis instead of just filling the void spaces among the nanofibrils. As a result, bundles of rutile nanotubes were obtained after the sample had been calcined in air at 800 °C. The thermodynamically stable rutile nanostructures were then explored as supports for Pt nanoparticles whose catalytic activity was evaluated using the reduction of *p*-nitrophenol by $NaBH_4$. The Pt supported on porous rutile fibers exhibited a better performance than the Pt on rutile nanotubes in terms of both induction time (t_{ind}) and apparent rate constant (k_{app}).

KEYWORDS: *titanium dioxide, rutile, platinum, porous nanostructure, tubular nanostructure*

1. INTRODUCTION

As one of the most studied materials over the past decades, titanium dioxide (TiO_2) still attracts enormous attention from the scientific community.[1] This is due to its incredible performance in a broad range of applications. This material has been commercialized as white pigments, primers for paints, additives in toothpastes, ointments, and sunscreens. It has also been demonstrated with great potential in niche applications such as photocatalysis, photovoltaics, electrochromics, and sensors, among others.[2−12] Owing to its superior physical, chemical, and thermal stabilities, TiO_2 has also been widely used as a supporting material for a variety of heterogeneous catalysts (e.g., Au, Pt, Pd, and Rh).[13−16] As a reducible oxide, TiO_2 can hold a remarkable amount of electronic defects on its surface, which are directly linked to the so-called strong metal−support interaction (SMSI).[17] The strong interaction between a metal catalyst and the surface defects of TiO_2 essentially determines the dispersion, morphology, and thus the activity and selectivity of the supported catalyst under various conditions.[14,18] For example, Yates and co-workers observed that dual catalytic sites were formed at the perimeter zone of Au nanoparticles supported on TiO_2. During CO oxidation, CO molecules first adsorbed onto the TiO_2 surface and then were delivered to the O_2-bound sites. Subsequently, the formation of the CO−O_2 complex at the interface of Au−TiO_2 activated the O−O bond scission. In comparison, the delivery rate of the CO/Au to the dual catalytic sites for the oxidation was much slower than that of CO/TiO_2. This study offers strong evidence to support the critical role of TiO_2 in promoting the catalytic activity of Au for CO oxidation at relatively low temperatures.[19] Additionally, it has been reported that strong oxides, including TiO_2 and CeO_2, are effective in stabilizing noble-metal nanoparticles against sintering by forming anchoring Ti (or Ce)−O−catalyst bonds.[15,16]

Numerous strategies have been developed for the synthesis of TiO_2 nanostructures. The methods include those based on sol−gel, micelle, hydrothermal, solvothermal, electrochemical anodization, electrodeposition, and chemical (or physical) vapor deposition. Accordingly, a variety of structures, such as particles, rods, wires, fibers, and tubes, have already been reported. However, most of these nanostructures were not specifically developed for applications as catalyst supports.[1,4,9,20−27] Therefore, some vital prerequisites in designing catalyst supports were not adequately addressed. These prerequisites include the controls over size, porosity, surface area, crystallinity, polymorph, structure, and stability.[28] Hierarchically porous nanostructures with an interconnected framework of nanoparticles have been shown as a promising candidate as the supports for heterogeneous catalysts. This can be attributed to their high surface area, high structural permeability, and good mechanical strength.[29,30] In spite of some successes, it remains a grand challenge to fabricate TiO_2

Received: April 26, 2013
Accepted: June 13, 2013
Published: June 13, 2013

dx.doi.org/10.1021/am4015633 | *ACS Appl. Mater. Interfaces* 2013, 5, 6391−6399

nanostructures with well-defined structure, porosity, grain size, and phase suitable for desired catalytic applications.

Herein, we demonstrate a facile approach to the synthesis of hierarchically structured TiO_2 nanomaterials via a templating method in combination with sol−gel deposition and calcination at high temperatures. A polystyrene (PS) yarn was employed as the template due to its potential in directing the deposition and supporting the growth of unique TiO_2 structures. The yarn was comprised of bundles of nanofibrils and covered by a predominantly solid skin with some tiny pores. By taking advantage of the void spaces among the nanofibrils and the surfaces of individual fibrils, we generated two kinds of nanostructures with porous and tubular structures, respectively. This was accomplished by maneuvering the surface wettability of the nanofibrils. Furthermore, the reaction parameters used in sol−gel deposition could also be varied and optimized for generating the desired substrates (i.e., interfibril voids vs fibril surfaces). Among the three common polymorphs of TiO_2 (anatase, brookite, and rutile), rutile is the most attractive for high-temperature catalytic applications (e.g., CO oxidation), which can be ascribed to its extraordinary thermodynamic stability.[1,31] However, the transformation from anatase to rutile typically occurs in the temperature range 600−800 °C.[32] At such high temperatures, the porous nanostructures tend to collapse, as caused by sintering and crystallization, leading to a damaged or densified product. This is probably the reason why most of the TiO_2 used as catalytic supports has only been examined in the anatase phase at temperatures below 700 °C.[22,33−37] Here we demonstrated that rutile nanostructures could be prepared with a well-preserved porous structure. Furthermore, the accessibility of catalysts (e.g., Pt) supported on the resultant TiO_2 can be readily evaluated by measuring the kinetics of a model reaction.

2. EXPERIMENTAL SECTION

2.1. Fabrication of Yarns Comprised of PS Nanofibrils. The yarns of PS nanofibrils were prepared by electrospinning a 20 wt % solution of PS (average $M_w \approx 350\,000$, average $M_n \approx 170\,000$) in anhydrous *N*,*N*-dimethylformamide (DMF, 99.8%, Aldrich) at 20 °C and a relative humidity of 52%.[38] In a typical procedure, the PS solution was loaded into a 3 mL syringe fitted with a 23-gauge inner diameter and ca. 2.5 cm long flat metal needle (BD Medical) and delivered at 1 mL/h by using a syringe pump (KDS 200, KD Scientific). A voltage of 15 kV from a DC power source (ES 30-0.1 P, Gamma High Voltage Research) was applied to the vertically positioned needle. The charged jet was spun into yarns of nanofibrils and collected on a piece of aluminum foil plate (20 cm × 20 cm) placed ca. 25 cm below the tip of the needle. The as-prepared nonwoven mat of PS yarns was dried at ambient temperature under a vacuum for 24 h prior to the subsequent characterization and solution deposition.

2.2. Fabrication of TiO_2 Nanostructures. The porous fiber of TiO_2 (*p*-TiO_2) was prepared by infiltrating a precursor solution into the void spaces among PS nanofibrils in each yarn, followed by calcination in air at an elevated temperature to remove the polymer phase, as well as to convert the amorphous TiO_2 into a crystalline structure. In a typical procedure, a mat of pristine PS yarns (L × W × H: 30 mm × 30 mm × 3 mm) was immersed in 10 mL of 5 wt % $Ti(OiPr)_4$ (99.999%, Aldrich) solution in a mixture of ethanol and acetic acid (EtOH/HAc: 5/14, v/v). The coating was conducted by agitating the reaction solution at room temperature (20 °C) with an orbit shaker (Orbit 300, LabNet) at 300 rpm for 24 h, followed by filtration to remove the remaining reagents. The hydrolysis was continued for another 12 h in air at room temperature. The sample was subsequently calcined at 800 °C in air for 2 h at a ramp rate of 10 °C/min to remove the organic components and transform the amorphous TiO_2 into rutile. The bundle of TiO_2 nanotubes (*t*-TiO_2) was fabricated by forming conformal coatings of TiO_2 on the surfaces of nanofibrils in each yarn. To accomplish, we had to transform the PS nanofibrils from hydrophobic to hydrophilic by treating with plasma (PDC-001, Harrick Plasma) for 20 min. A piece of the treated mat (L × W × H: 30 mm × 30 mm × 3 mm) was immediately immersed into 10 mL of $Ti(OiPr)_4$ reaction solution, followed by heating at 40 °C for 24 h. The sample was then washed five times with ethanol to remove the remaining reagents and air-dried at room temperature. Finally, the product was converted to rutile by calcination in air at 800 °C for 2 h. The sample comprised of a mixture of porous and tubular nanostructures of rutile was obtained by coating a plasma-treated PS mat at room temperature instead of 40 °C. All the other parameters and operations were kept the same as those used in the preparation of porous or tubular nanostructures.

2.3. Synthesis of Pt Nanoparticles. Pt nanoparticles with an average diameter of 3.4 ± 0.6 nm were synthesized using a polyol reduction method.[39,40] Typically, 4 mL of ethylene glycol (EG, J.T. Baker, 9300-01) was added into a glass vial and heated in an oil bath at 110 °C for 30 min. Meanwhile, poly(vinyl pyrrolidone) (PVP) (22.5 mg, $M_w \approx 55\,000$, Aldrich) and H_2PtCl_6 (16.5 mg, 99.995%, Aldrich) were dissolved separately in 2 mL of EG at room temperature. Subsequently, 0.5 mL of each solution was added simultaneously into the preheated EG at a rate of 0.67 mL/min. The reaction was continued at 110 °C for 4 h and finally cooled down to room temperature. The as-prepared Pt nanoparticles were thoroughly washed with acetone and ethanol, and then redispersed in ethanol to form the stocking solution for the following experiments.

2.4. Loading of Pt Nanoparticles onto the Porous and Tubular TiO_2 Nanostructures. In a typical experiment, 1.7 mg of the porous (or tubular) TiO_2 nanostructures were added into 5 mL of ethanol and dispersed by sonication for 10 min. 50 μL of the Pt stocking suspension was introduced, and the solution was stirred overnight at room temperature. The as-prepared Pt/TiO_2 was collected by centrifugation at 5000 rpm, and the loosely bound Pt nanoparticles were removed through extensive ethanol washing.

2.5. Catalytic Activity Measurement. We chose the reduction of *p*-nitrophenol by sodium borohydride ($NaBH_4$) as a model reaction to quantitatively evaluate the catalytic activity of the Pt/porous TiO_2 (Pt/*p*-TiO_2) and Pt/tubular TiO_2 (Pt/*t*-TiO_2). The aqueous solutions of *p*-nitrophenol (99%, Aldrich) and $NaBH_4$ (99.99%, Aldrich) should be freshly prepared before each use. In a typical assay, 50 μL of *p*-nitrophenol (7.4 mM), 50 μL of $NaBH_4$ (2.4 M), and 2.5 mL of water purified by a Milli-Q system (18.2 MΩ) were mixed in a 3.5 mL UV quartz cuvette. Then, 1.4 mg of Pt/*p*-TiO_2 or Pt/*t*-TiO_2 was added into the solution to initiate the reaction. The initial concentrations of *p*-nitrophenol, $NaBH_4$, and Pt were set to 1.42×10^{-4}, 4.62×10^{-2}, and 3.2×10^{-5} M, respectively, in the reaction mixture. The reaction kinetics was measured by recording the extinction peak of *p*-nitrophenol at 400 nm using a UV−vis spectrometer (Cary 50, Varian).

2.6. Characterization. The surface morphology and the structure porosity of the samples were examined using a scanning electron microscope (SEM, Nova 200, FEI) after gold coating for 60 s (Bio-Rad). The images were taken at an accelerating voltage of 15 kV and a working distance of 5 mm. The diameters of fibers, particles, and tubes were measured using the ImageJ software and then statistically analyzed using Origin 8 (OriginLab). TEM images were captured using a Tecnai G2 Sprit Twin (FEI) operated at an accelerating voltage of 120 kV. All samples were prepared by adding a drop (1.5 μL) of the final product dispersed in ethanol onto a carbon-coated copper grid and dried under ambient conditions. The crystalline phases were determined by X-ray diffraction (XRD), with a Rigaku Geigerflex D-MAX/A Diffractometer, of the powder samples at 45 kV and 40 mA from 20 to 80° with a Ni-filtered Cu Kα radiation (λ = 1.542 Å). Both the UV−vis scan and the kinetics spectra were recorded using a Cary 50 UV−vis spectrophotometer (Varian). An inductively coupled plasma mass spectrometer (ICP-MS, ELAN DRC II, PerkinElmer) was used to determine the concentration of Pt.

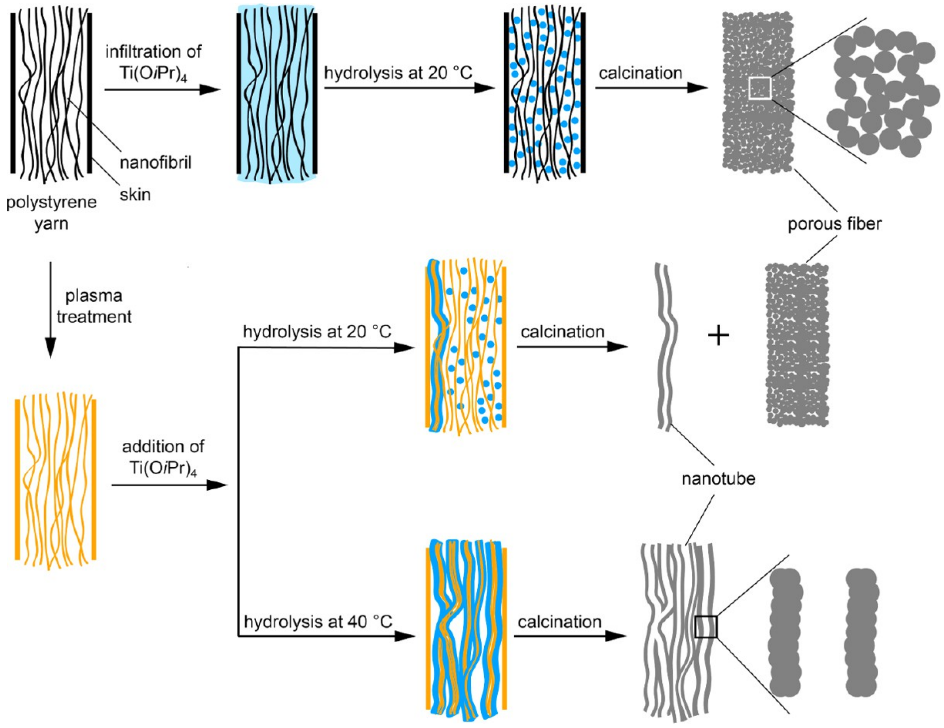

Figure 1. A schematic illustration of the methods used for generating porous and tubular TiO_2 nanostructures by templating against electrospun yarns made of polystyrene nanofibrils. The drawing is not proportional to the actual size/shape.

3. RESULTS AND DISCUSSION

3.1. Synthesis of Porous Fibers and Nanotubes of TiO_2. We used a template-assisted route to synthesize both porous and tubular nanostructures of TiO_2 by employing PS yarns as the templates. The pattern of TiO_2 deposition was controlled by maneuvering the surface wettability of PS yarns and using proper reaction conditions. As shown in Figure 1, the Ti(O*i*Pr)$_4$ solution in a mixture of ethanol and acetic acid (5:14, v:v) could be infiltrated into a mat of PS yarns under vigorous agitation. Without plasma treatment, both the PS yarn and nanofibrils maintained their hydrophobic character that prevented the sol−gel solution from wetting the surface of individual nanofibrils. During hydrolysis, TiO_2 was generated in the void spaces among nanofibrils and the solid skin could serve as a physical barrier to retain the resultant TiO_2 nanoparticles. After removal of the PS yarns by calcination in air, porous fibers consisting of an interconnected network of nanoparticles were obtained. If plasma treatment was applied, however, the surfaces of nanofibrils and the outer skin were transformed from hydrophobic to hydrophilic. In addition, some highly reactive sites were likely introduced due to the generation of radicals during plasma treatment. These changes facilitated the deposition of TiO_2 onto the surfaces of individual nanofibrils as conformal coatings. After removal of PS by calcination, bundles of TiO_2 nanotubes were produced.

The yarns made of PS nanofibrils were fabricated by electrospinning a 20 wt % PS DMF solution at an optimized condition (relative humidity, 52%; temperature, 20 °C) via a vapor-induced phase separation.[38] The PS yarns with an average diameter of 1.94 ± 0.07 μm were composed of many fibrils with sizes around 50 nm and a solid skin (Figure 2A). By following the above routes described in Figure 1, two different types of yarns were used, one without plasma treatment (or the pristine sample) and the other with plasma treatment for 20 min. They were then used as templates for the synthesis of porous and tubular TiO_2, respectively. Figure 2B shows cross sections of the pristine sample after reacting with Ti(O*i*Pr)$_4$ at room temperature (20 °C) for 24 h. The inset clearly shows that the hydrolyzed TiO_2 nanoparticles filled the interfibril void spaces of each yarn, demonstrating the capability of the solid skin in entrapping particles. On the contrary, we observed that TiO_2 was mainly deposited on the surfaces of nanofibrils as conformal, uniform coatings after the surfaces had been transformed into hydrophilic by using plasma treatment. This was evidenced by the open interfibril pores after TiO_2 deposition (Figure 2C,D). It is worth noting that the plasma-treated sample immediately turned light brown after immersing into the reaction solution. In contrast, the sample without plasma did not change its white color. Furthermore, the PS yarns kept their smooth surfaces and no TiO_2 nanoparticles were deposited on the skin of the PS yarn (Figure S1, Supporting Information).

The TiO_2/PS composites were converted to crystalline TiO_2 by calcination in air at 800 °C for 2 h with a ramp rate of 10 °C/min. By reacting the pristine PS yarns with 5% Ti(O*i*Pr)$_4$ solution, we obtained highly porous TiO_2 fibers with an average diameter of 1.5 ± 0.1 μm after calcination (Figure 3A). The porous TiO_2 fiber was comprised of nanoparticles with diameters in the range 20−80 nm, which matched the lateral dimensions of the interfibril void spaces. These nanoparticles were fused together at their contacting sites to generate an interconnected network, in which the interparticle pores are clearly visible (Figure 3A, inset). By varying the concentration of Ti(O*i*Pr)$_4$ from 1.25 to 15%, we obtained several different types of TiO_2 structures after calcination. These included solid fibers, porous fibers, and porous core/sheath fibers (Figure S2, Supporting Information). Solid fibers with an average diameter of 446 ± 49 nm, made of densely sintered particles, were obtained when 1.25% Ti(O*i*Pr)$_4$ solution was used (Figure

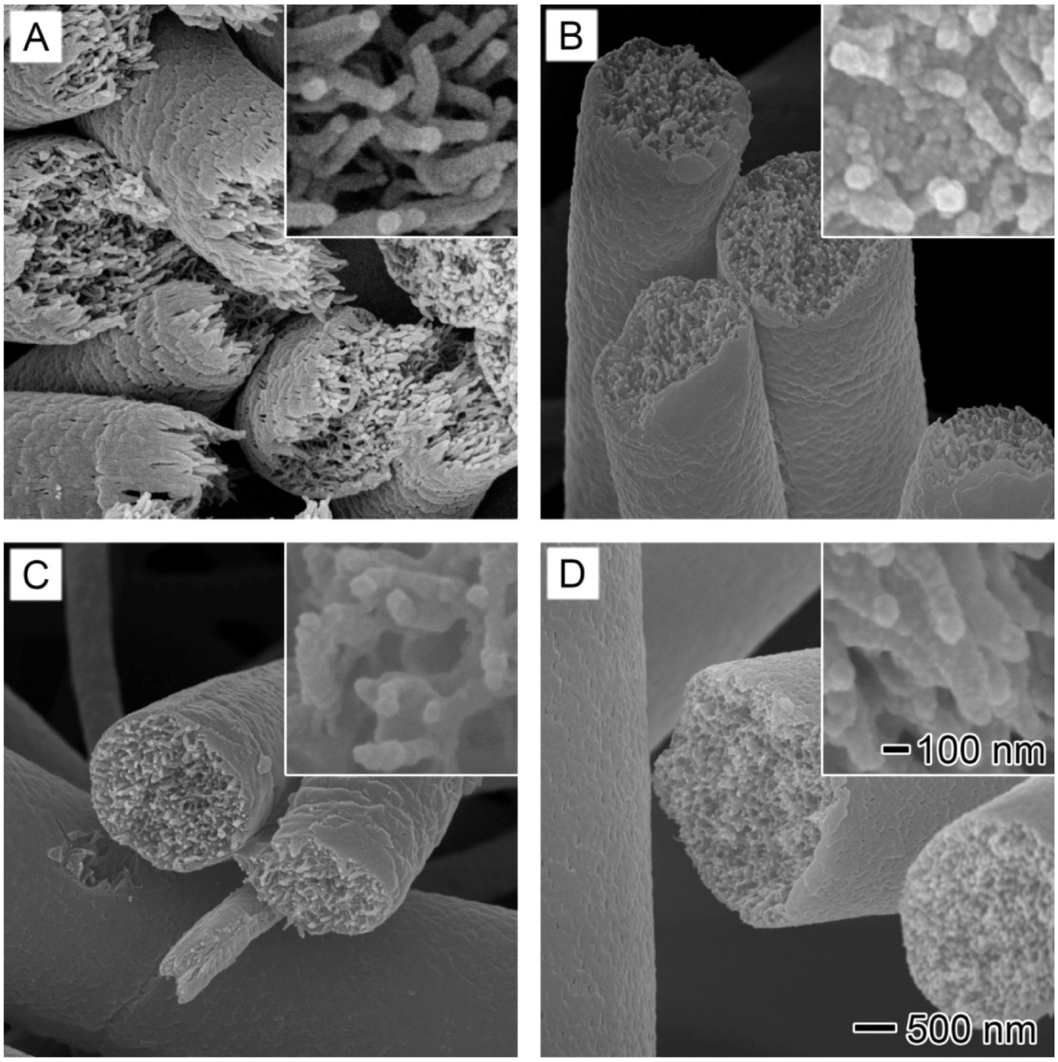

Figure 2. SEM images showing the PS yarns consisting of many nanofibrils (A) before and (B–D) after reacting with 5% Ti(O*i*Pr)$_4$ solution in a mixture of ethanol and acetic acid (5:14, v:v). The deposition reaction was performed at (B, C) room temperature (20 °C) and (D) 40 °C for (B) pristine and (C, D) plasma-treated PS yarns. The scale bars in part D and its inset also apply to other images and insets.

S2A, Supporting Information). Furthermore, sintering was observed among the fibers. We observed fusion and coalescence of the fibers along their long axes for fibers in parallel or at the intersections for overlapping fibers. By increasing the concentration of Ti(O*i*Pr)$_4$ to 2.5%, a mixture of solid and porous fibers was generated (Figure S2B, Supporting Information). Porous fibers with exposed interparticle porosity became the only product when a 5% Ti(O*i*Pr)$_4$ solution was used (Figure 3A). By further increasing the concentration of Ti(O*i*Pr)$_4$ to 10%, porous core/sheath TiO$_2$ fibers were obtained. They contained a porous fiber as the core and a solid layer as the sheath (Figure S2C, Supporting Information). Compact core/sheath TiO$_2$ fibers were generated with a further increase of the concentration of Ti(O*i*Pr)$_4$ to 15% (Figure S2D, Supporting Information). From these results, it was evident that the concentration of precursor played an essential role in determining the structure and morphology of the final product. At low Ti(O*i*Pr)$_4$ concentration (e.g., 1.25%), only a limited amount of TiO$_2$ was trapped inside the yarn. It subsequently went through a rapid shrinkage with the PS template during calcination, leading to the formation of solid fibers. The feasibility of generating an interconnected network became realistic only when the interior loading of TiO$_2$ reached a threshold value. At this point, the hydrolyzed particles were able to touch each other along different directions to prevent collapse. With a further increase of precursor concentration, not only the interfibril spaces but also the inner wall of the sheath could be deposited with the hydrolyzed TiO$_2$. As such, we obtained a porous core/sheath structure after the removal of PS. The above analyses on the formation of TiO$_2$ structures were supported by the experiment results. They also agreed well with the hydrophobic property of PS and the porous characteristic of a yarn structure.

A 20 min plasma treatment altered the surface property of PS yarns from hydrophobic to hydrophilic. This transformation was evidenced by the rapid wetting of the sample by water. Furthermore, some chemically active sites were probably produced on the surfaces of both nanofibrils and yarns due to the reactive nature of plasma. An immediate color change from white to light brown was observed for the sample upon contacting with Ti(O*i*Pr)$_4$ solution. An intermediate between porous and tubular TiO$_2$ was observed after calcination, as shown in Figure 3B. It was possibly associated with the incomplete deposition of TiO$_2$ on the nanofibrils due to the

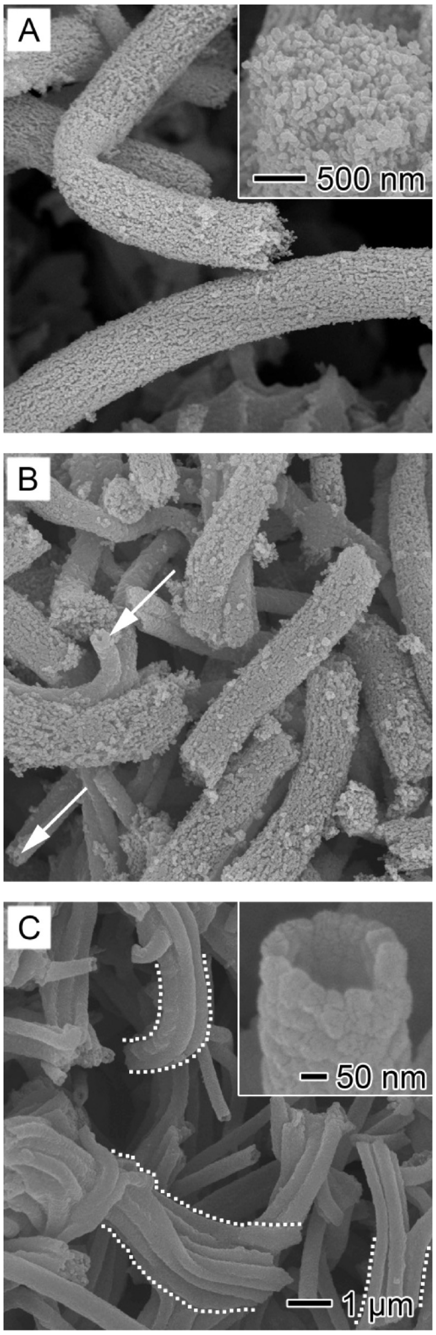

Figure 3. SEM images showing (A) porous, (B) a mixture of porous and tubular, and (C) tubular nanostructures of TiO_2 obtained via calcination of the corresponding TiO_2/PS samples in Figure 2. The arrows in part B point to the scattered tubular TiO_2. The dashed curves in part C sketch out the bundles of tubes. The scale bar in part C also apples to other images.

low reactivity at room temperature. In order to improve the surface deposition, the hydrolysis temperature was raised to 40 °C. The as-prepared TiO_2/PS composite fibers are shown in Figure 2D. It is clear that the interfibril void spaces were well retained and only the surfaces of the nanofibrils were coated with conformal sheaths. Additionally, the composite fibers became more brittle than the original PS yarns or the particle-filled PS, as illustrated by the broken yarns in Figure S1C (Supporting Information). This probably resulted from the increased rigidity after the deposition of TiO_2 onto the nanofibrils. This speculation was confirmed by the formation of tubular TiO_2 after calcination (Figure 3C). Intriguingly, the resultant nanotubes of TiO_2 were almost 4 times bigger than the template nanofibrils (~50 nm) in each PS yarn, with an inner diameter (ID) of 216 ± 36 nm and an outside diameter (OD) of 365 ± 51 nm. This can probably be attributed to the tight entanglement and binding among nanofibrils. Furthermore, the nanotubes of TiO_2 were presented as bundles (see dotted lines in Figure 3C). These results confirmed that TiO_2 was coated on the surfaces of nanofibrils instead of the outer surface of a yarn. By further increasing the reaction temperature to 60 °C, the whole PS mat shrunk substantially and only TiO_2 fragments were produced after calcination (Figure S3, Supporting Information). This was possibly caused by the deformation of PS yarns or a rapid deposition rate for the TiO_2 phase.

The internal structures of porous and tubular TiO_2 were examined by TEM. Figure 4A shows a portion of the porous TiO_2 fibers with a diameter of ca. 1.5 μm. Nanoparticles with irregular shapes and an average size of 48 ± 17 nm were assembled into an elaborate network full of interparticle pores. The porous TiO_2 demonstrated exceptional structural stability by maintaining its integrity after 30 min of vigorous sonication in water. This could be attributed to the fusion of contacting sites among nanoparticles via high-temperature sintering. On the contrary, the walls of tubular TiO_2 were made of densely packed nanoparticles, leaving behind very little interparticle space (Figure 4B).

The change of sample crystalline structures during calcination was monitored using XRD. The samples before heating, including the PS yarns, air-dried $Ti(OiPr)_4$, and TiO_2/PS composites, are generally featureless except for a broad band below a 2θ angle of 30° (Figure 5A−C and H). It is characteristic of amorphous materials. The sample was converted to anatase after calcination at 500 °C for 2 h, manifested by its representative peaks at 2θ = 25.3, 37.8, 48.1, 53.9, 55.1, 62.7, 68.9, 70.2, and 75.0°. These peaks corresponded to the (101), (004), (200), (105), (211), (204), (116), (220), and (215) planes of anatase, respectively (PDF No. 01-086-1157) (Figure 5D).[4,22,24] Furthermore, the disappearance of the broad band below 30° in the diffraction pattern indicated a complete removal of the amorphous PS. A small peak showed up at 2θ = 27.3° when the calcination temperature was increased to 600 °C. It can be assigned to the (110) plane of rutile, which indicated the initiation of the phase transition from anatase to rutile (Figure 5E). This transformation was confirmed by a further increase in the peak intensity of (110) at 2θ = 27.3° for the sample calcined at 700 °C. Meanwhile, other characteristic peaks of rutile appeared at 35.9, 39.0, 41.1, 43.9, 54.2, 56.5, 62.6, 64.0, 68.9, 69.6, and 76.4°. These peaks could be designated to the (101), (200), (111), (210), (211), (220), (002), (310), (301), (112), and (202) planes of rutile (PDF No. 04-0087847), respectively.[6,31] Additionally, the characteristic (101) peak of anatase at 2θ = 25.3° was greatly weakened, suggesting the decrease of anatase fraction in the sample (Figure 5F and I). After calcination at 800 °C for 2 h, the biphasic TiO_2 was completely converted into rutile phase (Figure 5G and J), which agreed well with the previous report.[32]

3.2. Evaluation of the Performance of Porous and Tubular TiO_2 as Catalyst Supports. The porous and tubular TiO_2 nanostructures were mechanically strong and chemically stable, making them good supporting materials for catalysts.

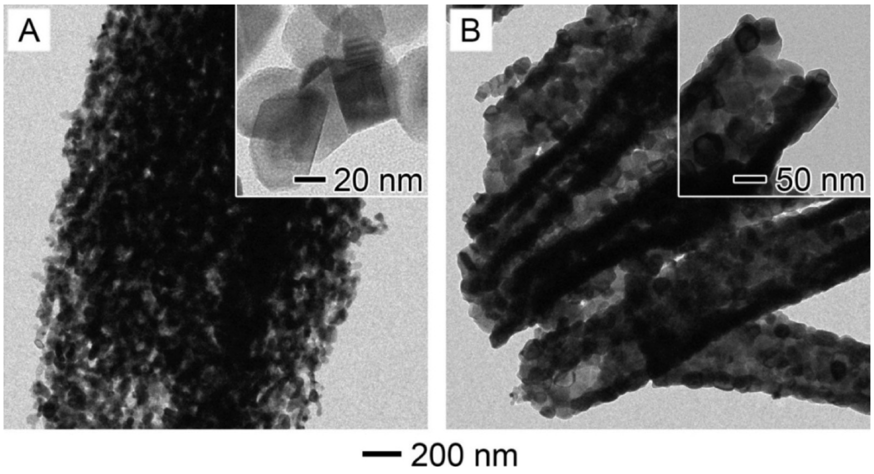

Figure 4. TEM images showing (A) porous and (B) tubular nanostructures of rutile obtained via calcination of the corresponding TiO_2/PS composite samples in air at 800 °C for 2 h.

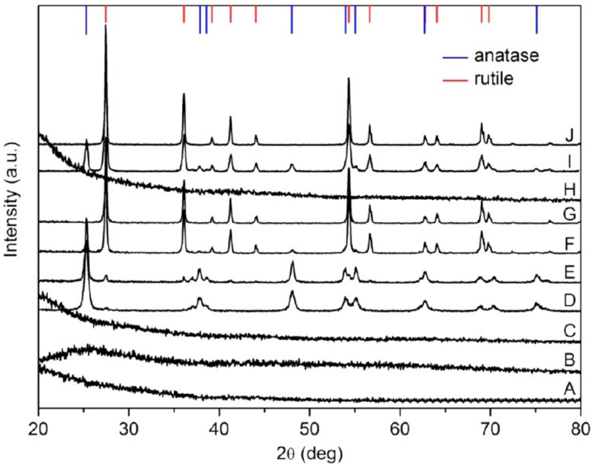

Figure 5. X-ray powder diffraction patterns of (A) PS yarns, (B) air-dried $Ti(O\textit{i}Pr)_4$, and (C) TiO_2/PS composites (without plasma treatment, hydrolyzed at 20 °C) and the corresponding products after calcination in air at (D) 500 °C, (E) 600 °C, (F) 700 °C, and (G) 800 °C. (H–J) The TiO_2/PS composites (with plasma treatment, hydrolyzed at 40 °C) before and after calcination at (I) 700 °C and (J) 800 °C are also provided for comparison.

The activity of a catalyst supported on TiO_2 was determined by the diffusion kinetics of substrate or product through the supporting framework. We chose Pt nanoparticles with an average diameter of 3.4 ± 0.6 nm (Figure S4, Supporting Information) as a model catalyst in this study. They were synthesized using a polyol reduction reaction reported in our previous publications.[39,40] The as-synthesized Pt nanoparticles demonstrated a strong interaction with the porous and tubular TiO_2. We did not observe particle desorption from the TiO_2 nanostructures under vigorous sonication and washing. Furthermore, the Pt nanoparticles were distributed across the surface of interconnected particles in the porous TiO_2 or the external and/or internal walls of the tubular TiO_2 without agglomeration (Figure 6). The final Pt loadings on the porous and tubular TiO_2 were 1.32 and 1.29%, respectively.

The catalytic activity and reaction kinetics of Pt nanoparticles supported on TiO_2 (Pt/TiO_2) were quantitatively evaluated using the reduction of *p*-nitrophenol to *p*-aminophenol by $NaBH_4$. This model reaction was demonstrated to be a reliable and convenient method in assessing the catalytic activity of Pt nanoparticles.[41−44] Aqueous *p*-nitrophenol solution in a faint yellow color showed a median absorption peak centered at 317 nm, which was immediately red-shifted to 400 nm upon the

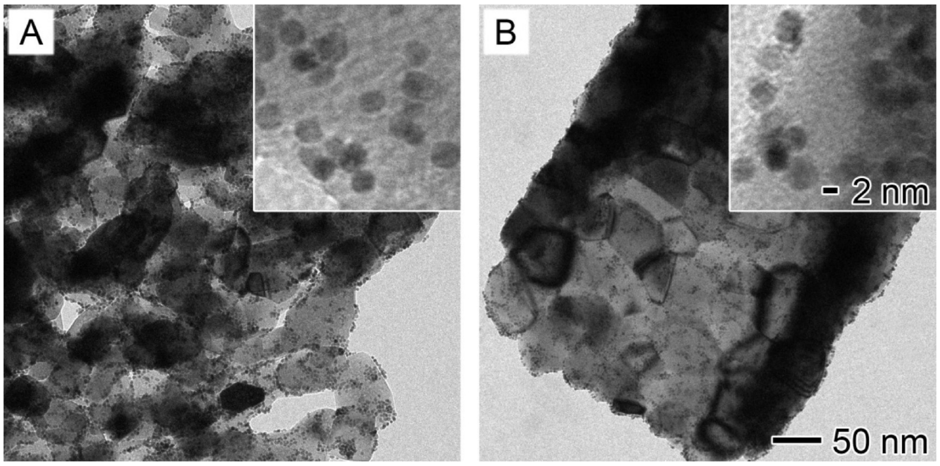

Figure 6. TEM images showing (A) porous and (B) tubular TiO_2 nanostructures deposited with Pt nanoparticles (Pt loading: 1.32% for porous and 1.29% for tubular TiO_2, respectively). The scale bars in part B also apply to part A.

addition of $NaBH_4$ (Figure S5, Supporting Information). Furthermore, the peak at 400 nm was doubled in intensity as compared to that of the peak at 317 nm. Meanwhile, the solution also changed to a brilliant yellow color from a faint yellow color. The peak shift was believed to be associated with the formation of *p*-nitrophenolate ions in the basic $NaBH_4$ solution.[44−46] Figure 7A shows a series of time-dependent UV−vis spectra of the reaction solution upon the addition of Pt nanoparticles (3.2×10^{-5} M). The extinction peak of *p*-nitrophenol (or *p*-nitrophenolate) at 400 nm decreased in a decelerated fashion until an equilibrium was attained. Figure 7B shows the normalized extinction at 400 nm that was recorded for reaction solutions at time zero upon introducing the TiO_2, Pt nanoparticles, Pt/porous TiO_2 (Pt/*p*-TiO_2), and Pt/tubular TiO_2 (Pt/*t*-TiO_2). We confirmed that the reduction of *p*-nitrophenol to *p*-aminophenol by $NaBH_4$ did not occur by adding only the porous or tubular TiO_2 nanostructures (Figure 7B,C). In the reaction solution, the concentrations of *p*-nitrophenol and $NaBH_4$ were 1.42×10^{-4} and 4.62×10^{-2} M, respectively. Since the concentration of $NaBH_4$ greatly exceeded that of *p*-nitrophenol, it was rational to assume the concentration of BH_4^- to be constant during the reaction. Therefore, the pseudo-first-order kinetics with respect to *p*-nitrophenol could be applied to calculate the apparent rate constant (k_{app}). The approximately linear plots of $-\ln I_{ext}$ (400 nm) against the reaction time supported the pseudo-first-order assumption (Figure 7C). We found that an induction period (t_{ind}, the initial flat region in Figure 7C) was required before the reaction could be initiated. This induction time was probably associated with the diffusion and adsorption of *p*-nitrophenol onto the metal surface. Additionally, in order to make the calculated k_{app} values comparable between catalysts, the concentrations of Pt were controlled to be 3.2×10^{-5} M in the reaction solution for all three Pt-based catalysts.

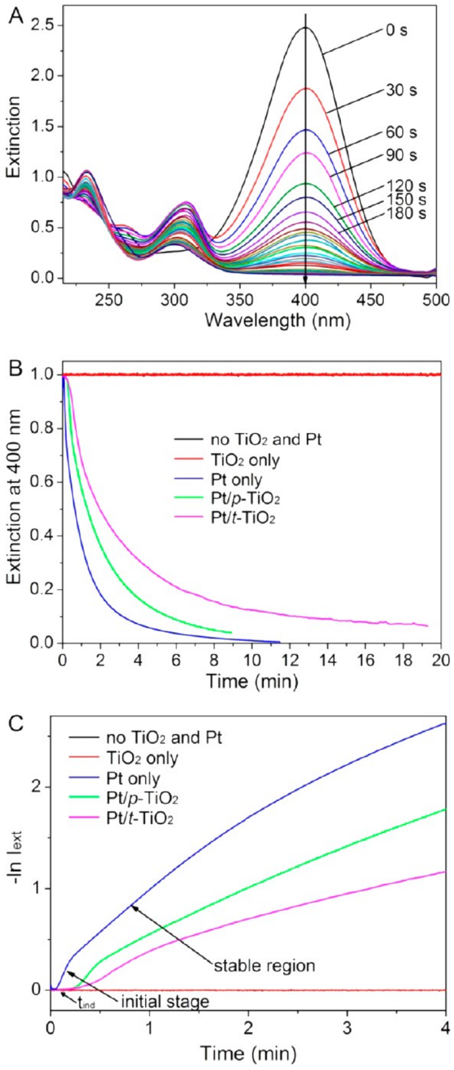

Figure 7. (A) UV−vis spectra showing the decrease of extinction peak at 400 nm associated with the reduction of *p*-nitrophenol by $NaBH_4$ in the presence of Pt nanoparticles (3.2×10^{-5} M), recorded at a time interval of 30 s. (B) The normalized extinction at 400 nm for the reaction solution as a function of time after the addition of TiO_2, Pt nanoparticles, Pt/*p*-TiO_2, and Pt/*t*-TiO_2. (C) Plots of $-\ln I_{ext}$ (400 nm) against the reaction time that were employed to determine the induction time (t_{ind}) and derive the apparent rate constant (k_{app}).

The measured t_{ind} and the best-fit k_{app} are summarized in Table 1. The free Pt nanoparticles, Pt/*p*-TiO_2, and Pt/*t*-TiO_2 demonstrated comparable t_{ind}, which indicates their similar accessibility to reactive species. We noticed that the reductions by the three Pt-based catalysts all displayed a bimodal curve (Figure 7C). It consisted of a faster increase at the initial stage and a slower raise in the following region, probably associated with the formation of an intermediate product. Further studies are necessary for a better understanding of the reaction mechanism. Therefore, the values of k_{app} at both regions, referred to as the initial stage and the stable region, were derived from the corresponding portion of the curves for comparison. It was clear that the initial stage would have a larger k_{app} value than the stable region, manifested by the decreased slope of the curve after passing the bimodal point. At the initial stage, the Pt nanoparticles exhibited the highest k_{app} of 2.23 ± 0.10 min^{-1}. The Pt/*p*-TiO_2 and Pt/*t*-TiO_2 retained 55 and 25% of the k_{app} value of free Pt, respectively. The three catalysts showed a similar trend for the k_{app} values in the stable region. They were calculated to be 0.83 ± 0.06, 0.48 ± 0.04, and 0.26 ± 0.03 min^{-1} for Pt, Pt/*p*-TiO_2, and Pt/*t*-TiO_2, respectively. The k_{app} values in both the initial stage and the stable region, together with the values of t_{ind}, confirmed that the Pt/*p*-TiO_2 had a higher catalytic activity than the Pt/*t*-TiO_2. Specifically, the Pt/*p*-TiO_2 retained 55−58% of the k_{app} value of free Pt, while the Pt/*t*-TiO_2 only kept 25−31%. The Pt/*p*-TiO_2 also demonstrated a 20% faster diffusion kinetics than the Pt/*t*-TiO_2.

Table 1. Summary of the Induction Time (t_{ind}) and Reaction Rate Constant (k_{app}) at the Initial Stage and in the Stable Region for TiO_2, Pt, Pt/*p*-TiO_2, and Pt/*t*-TiO_2

sample	t_{ind} (min)	k_{app} (min^{-1}) initial stage	k_{app} (min^{-1}) stable region
TiO_2	n/a	0	0
Pt	0.05 ± 0.01	2.23 ± 0.10	0.83 ± 0.06
Pt/*p*-TiO_2	0.15 ± 0.03	1.22 ± 0.04	0.48 ± 0.04
Pt/*t*-TiO_2	0.18 ± 0.01	0.56 ± 0.01	0.26 ± 0.03

4. CONCLUSIONS

In summary, we have demonstrated a facile approach to the synthesis of porous and tubular TiO_2 nanostructures by maneuvering the surface property of PS yarns and the reaction temperature. The PS yarn consisted of many nanofibrils with diameters around 50 nm, together with a solid skin. When the original hydrophobic PS yarns were used as the template, we obtained TiO_2/PS composites with TiO_2 entrapped in the void spaces among the nanofibrils. Porous fibers were produced after calcination, which were composed of interconnected rutile nanoparticles. The diameters of these nanoparticles were in the range 20−80 nm. After converting the PS yarns and nanofibrils to hydrophilic using plasma treatment, TiO_2 was deposited as conformal coatings onto the surfaces of nanofibrils instead of filling the interfibril void spaces during hydrolysis. As a result, bundles of rutile nanotubes were generated after calcination, which had an average inner diameter of 216 ± 36 nm and an outer diameter of 365 ± 51 nm. During calcination, we observed that TiO_2 went through a phase transformation from anatase to rutile in the temperature range 600−800 °C. The as-prepared nanostructures of rutile kept their well-defined porosity, making them immediately useful as supporting materials for Pt nanoparticles (3.4 ± 0.6 nm). The catalytic activities of supported Pt on TiO_2 were evaluated using the reduction of *p*-nitrophenol by $NaBH_4$. We observed that Pt/*p*-TiO_2 demonstrated a shorter t_{ind} than Pt/*t*-TiO_2 (0.15 ± 0.03 min vs 0.18 ± 0.01 min). Furthermore, the k_{app} values of Pt/*p*-TiO_2 derived from both the initial stage (1.22 ± 0.04 min^{-1}) and stable region (0.48 ± 0.04 min^{-1}) were larger than those of Pt/*t*-TiO_2 (0.56 ± 0.01 and 0.26 ± 0.03 min^{-1}), respectively. These hierarchically porous nanostructures of rutile are expected to find use in a variety of applications such as catalysis.

■ ASSOCIATED CONTENT

Ⓢ Supporting Information

SEM images of PS yarns, TiO_2/PS composites, and TiO_2 nanostructures by calcining the corresponding TiO_2/PS; TEM images of Pt nanoparticles and their size distribution; and UV−vis spectra showing the peak shift upon the addition of $NaBH_4$ to the aqueous solution of *p*-nitrophenol. This material is available free of charge via the Internet at http://pubs.acs.org.

■ AUTHOR INFORMATION

Corresponding Author

*E-mail: younan.xia@bme.gatech.edu.

Notes

The authors declare no competing financial interest.

■ ACKNOWLEDGMENTS

This work was supported in part by the NIH (R01 AR060820) and startup funds from Georgia Institute of Technology.

■ REFERENCES

(1) Chen, X.; Mao, S. S. *Chem. Rev.* **2007**, *107*, 2891−2959.

(2) Kim, H. I.; Moon, G. H.; Monllor-Satoca, D.; Park, Y.; Choi, W. *J. Phys. Chem. C* **2012**, *116*, 1535−1543.

(3) Lee, W. J.; Lee, J. M.; Kochuveedu, S. T.; Han, T. H.; Jeong, H. Y.; Park, M.; Yun, J. M.; Kwon, J.; No, K.; Kim, D. H.; Kim, S. O. *ACS Nano* **2012**, *6*, 935−943.

(4) Shang, S.; Jiao, X.; Chen, D. *ACS Appl. Mater. Interfaces* **2012**, *4*, 860−865.

(5) Boppella, R.; Basak, P.; Manorama, S. V. *ACS Appl. Mater. Interfaces* **2012**, *4*, 1239−1246.

(6) Guo, W.; Xu, C.; Wang, X.; Wang, S.; Pan, C.; Lin, C.; Wang, Z. L. *J. Am. Chem. Soc.* **2012**, *134*, 4437−4441.

(7) Liu, B.; Huang, Y.; Wen, Y.; Du, L.; Zeng, W.; Shi, Y.; Zhang, F.; Zhu, G.; Xu, X.; Wang, Y. *J. Mater. Chem.* **2012**, *22*, 7484−7491.

(8) Lu, X.; Wang, G.; Zhai, T.; Yu, M.; Gan, J.; Tong, Y.; Li, Y. *Nano Lett.* **2012**, *12*, 1690−1696.

(9) Qiu, J.; Zhuge, F.; Li, X.; Gao, X.; Gan, X.; Li, L.; Weng, B.; Shi, Z.; Hwang, Y. H. *J. Mater. Chem.* **2012**, *22*, 3549−3554.

(10) Ren, Y.; Liu, Z.; Pourpoint, F.; Armstrong, A. R.; Grey, C. P.; Bruce, P. G. *Angew. Chem., Int. Ed.* **2012**, *51*, 2164−2167.

(11) Shao, F.; Sun, J.; Gao, L.; Yang, S.; Luo, J. *J. Mater. Chem.* **2012**, *22*, 6824−6830.

(12) Tao, L.; Xiong, Y.; Liu, H.; Shen, W. *J. Mater. Chem.* **2012**, *22*, 7863−7870.

(13) Kimura, K.; Naya, S. I.; Jin-nouchi, Y.; Tada, H. *J. Phys. Chem. C* **2012**, *116*, 7111−7117.

(14) Chen, M. S.; Goodman, D. W. *Science* **2004**, *306*, 252−255.

(15) Campbell, C. T.; Parker, S. C.; Starr, D. E. *Science* **2002**, *298*, 811−814.

(16) Park, J. B.; Graciani, J.; Evans, J.; Stacchiola, D.; Ma, S.; Liu, P.; Nambu, A.; Sanz, J. F.; Hrbek, J.; Rodriguez, J. A. *Proc. Natl. Acad. Sci. U.S.A.* **2009**, *106*, 4975−4980.

(17) Kwak, J. H.; Hu, J.; Mei, D.; Yi, C. W.; Kim, D. H.; Peden, C. H. F.; Allard, L. F.; Szanyi, J. *Science* **2009**, *325*, 1670−1673.

(18) Lopez, N.; Nørskov, J. K.; Janssens, T. V. W.; Carlsson, A.; Puig-Molina, A.; Clausen, B. S.; Grunwaldt, J. D. *J. Catal.* **2004**, *225*, 86−94.

(19) Yates, J. T.; Green, I. X.; Tang, W. J.; Neurock, M. *Science* **2011**, *333*, 736−739.

(20) Chen, B.; Lu, K. *Langmuir* **2012**, *28*, 2937−2943.

(21) Cheng, C.; Karuturi, S. K.; Liu, L.; Liu, J.; Li, H.; Su, L. T.; Tok, A. I. Y.; Fan, H. J. *Small* **2012**, *8*, 37−42.

(22) Dutta, S.; Patra, A. K.; De, S.; Bhaumik, A.; Saha, B. *ACS Appl. Mater. Interfaces* **2012**, *4*, 1560−1564.

(23) Liao, J. Y.; He, J. W.; Xu, H.; Kuang, D. B.; Su, C. Y. *J. Mater. Chem.* **2012**, *22*, 7910−7918.

(24) Tang, Y.; Wee, P.; Lai, Y.; Wang, X.; Gong, D.; Kanhere, P. D.; Lim, T.-T.; Dong, Z.; Chen, Z. *J. Phys. Chem. C* **2012**, *116*, 2772−2780.

(25) Wang, H. E.; Lu, Z. G.; Xi, L. J.; Ma, R. G.; Wang, C. D.; Zapien, J. A.; Bello, I. *ACS Appl. Mater. Interfaces* **2012**, *4*, 1608−1613.

(26) Zhang, D.; Wen, M.; Zhang, P.; Zhu, J.; Li, G.; Li, H. *Langmuir* **2012**, *28*, 4543−4547.

(27) Zheng, L.; Cheng, H.; Liang, F.; Shu, S.; Tsang, C. K.; Li, H.; Lee, S. T.; Li, Y. Y. *J. Phys. Chem. C* **2012**, *116*, 5509−5515.

(28) Wen, D.; Guo, S. J.; Zhai, J. F.; Deng, L.; Ren, W.; Dong, S. J. *J. Phys. Chem. C* **2009**, *113*, 13023−13028.

(29) Ding, Y.; Wang, Y.; Zhang, L.; Zhang, H.; Li, C. M.; Lei, Y. *Nanoscale* **2011**, *3*, 1149−1157.

(30) Xiao, F. *J. Mater. Chem.* **2012**, *22*, 7819−7830.

(31) Liao, Y.; Que, W.; Jia, Q.; He, Y.; Zhang, J.; Zhong, P. *J. Mater. Chem.* **2012**, *22*, 7937−7944.

(32) Hegazy, A.; Prouzet, E. *Chem. Mater.* **2011**, *24*, 245−254.

(33) Li, D.; McCann, J. T.; Gratt, M.; Xia, Y. *Chem. Phys. Lett.* **2004**, *394*, 387−391.

(34) Li, D.; McCann, J. T.; Xia, Y. *Small* **2005**, *1*, 83−86.

(35) Ostermann, R.; Li, D.; Yin, Y. D.; McCann, J. T.; Xia, Y. N. *Nano Lett.* **2006**, *6*, 1297−1302.

(36) Formo, E.; Lee, E.; Campbell, D.; Xia, Y. N. *Nano Lett.* **2008**, *8*, 668−672.

(37) Rudisill, S. G.; Wang, Z.; Stein, A. *Langmuir* **2012**, *28*, 7310−7324.

(38) Lu, P.; Xia, Y. *Langmuir* **2013**, *29*, 7070−7078.

(39) Chen, J.; Herricks, T.; Geissler, M.; Xia, Y. *J. Am. Chem. Soc.* **2004**, *126*, 10854−10855.

(40) Dai, Y. Q.; Lim, B.; Yang, Y.; Cobley, C. M.; Li, W. Y.; Cho, E. C.; Grayson, B.; Fanson, P. T.; Campbell, C. T.; Sun, Y. M.; Xia, Y. N. *Angew. Chem., Int. Ed.* **2010**, *49*, 8165−8168.

(41) Lee, J.; Park, J. C.; Song, H. *Adv. Mater.* **2008**, *20*, 1523−1528.

(42) Hoseini, S. J.; Rashidi, M.; Bahrami, M. *J. Mater. Chem.* **2011**, *21*, 16170−16176.

(43) Yu, T. Y.; Zeng, J.; Lim, B.; Xia, Y. N. *Adv. Mater.* **2010**, *22*, 5188−5192.

(44) Zeng, J.; Zhang, Q.; Chen, J.; Xia, Y. *Nano Lett.* **2009**, *10*, 30−35.

(45) Hayakawa, K.; Yoshimura, T.; Esumi, K. *Langmuir* **2003**, *19*, 5517−5521.

(46) Praharaj, S.; Nath, S.; Ghosh, S. K.; Kundu, S.; Pal, T. *Langmuir* **2004**, *20*, 9889−9892.